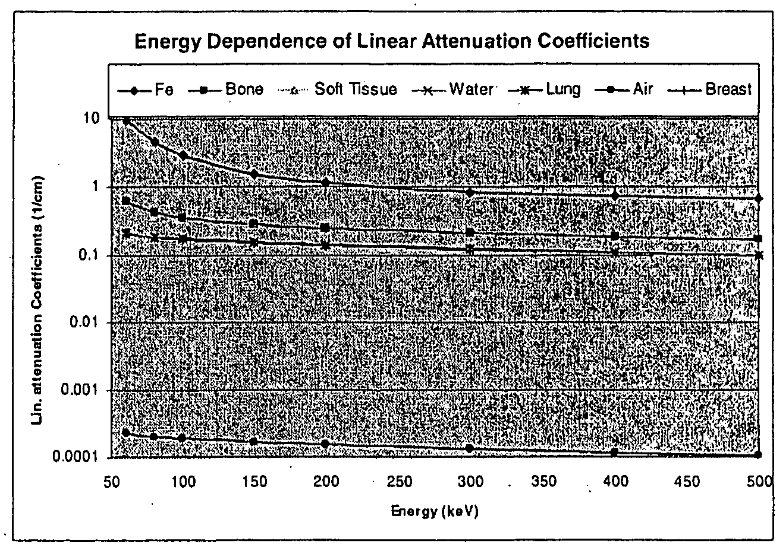

Figure 1: Energy dependence of linear attenuation coefficients for various tissues and Iron. The graph shows that various soft tissu, bone, and iron form three distinct classes.

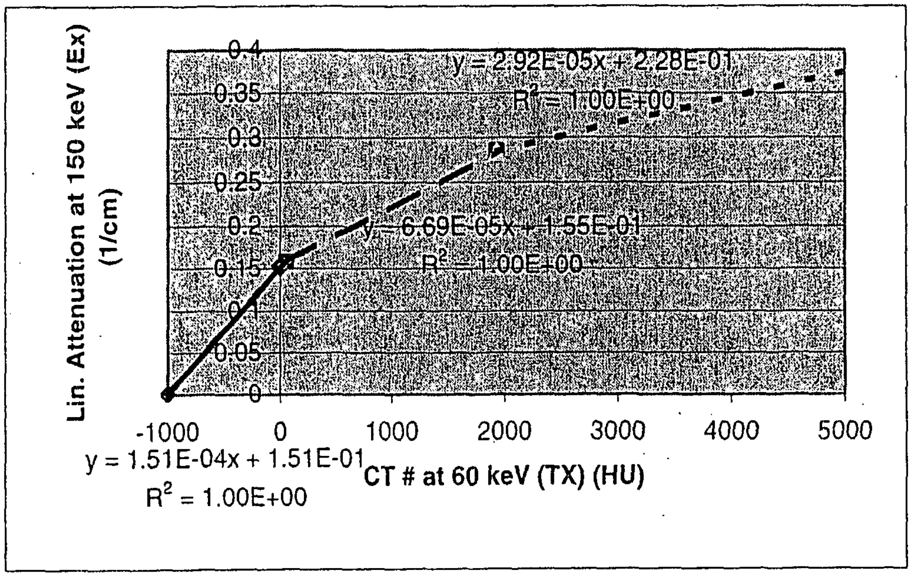

Figure 2: Typical conversion graph from HU to linear attenuation coefficients at 60 keV transmission energy and 150 keV emissions energy.

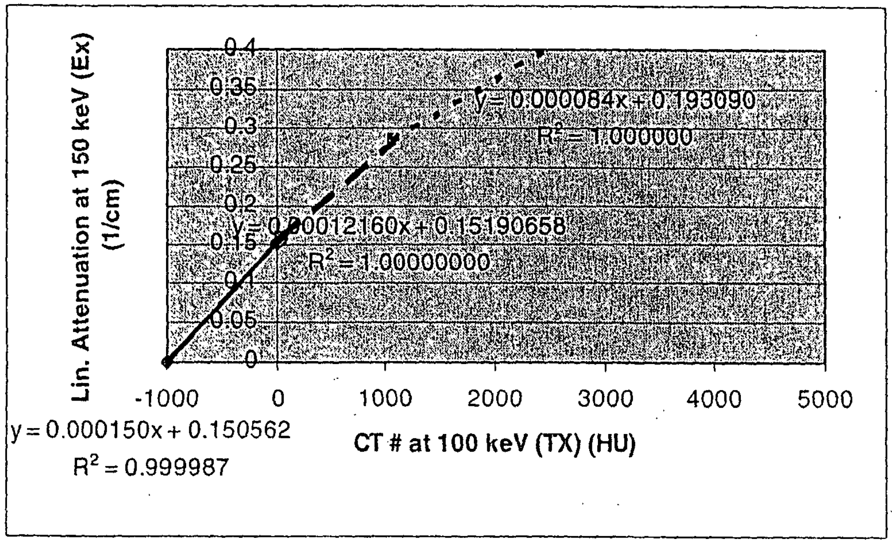

Figure 3: Typical conversion graph from HU to linear attenuation coefficients at 100 keV transmission energy and 150 keV emissions energy.

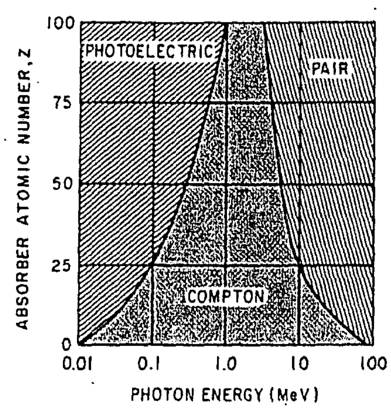

Figure 4: Most prominent interaction for biological materials (Z=1 ...Z=20) and relevant energies (50 keV – 511 keV). For low Z it is Compton scattering (SP80).

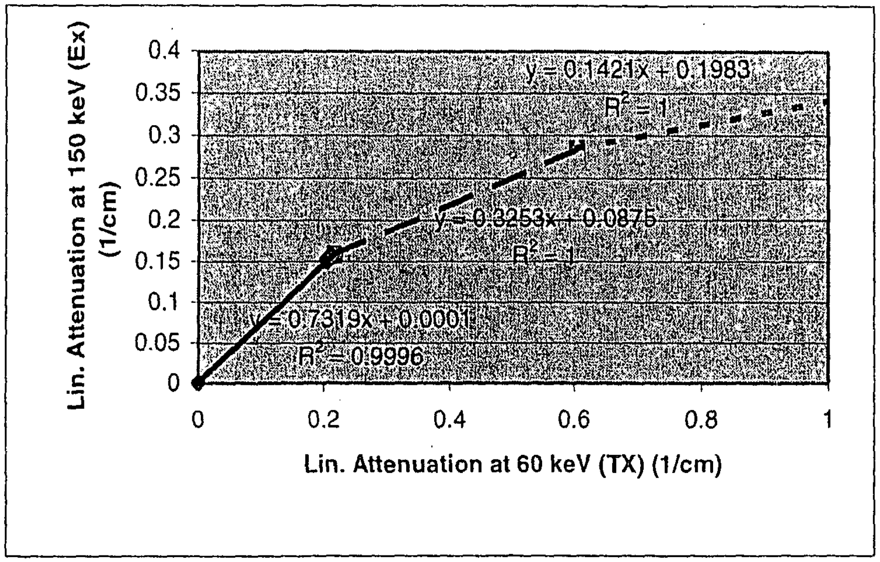

Figure 5: Conversion from HU to minear attenuation coefficients can be approximated as piecewise linear functions.

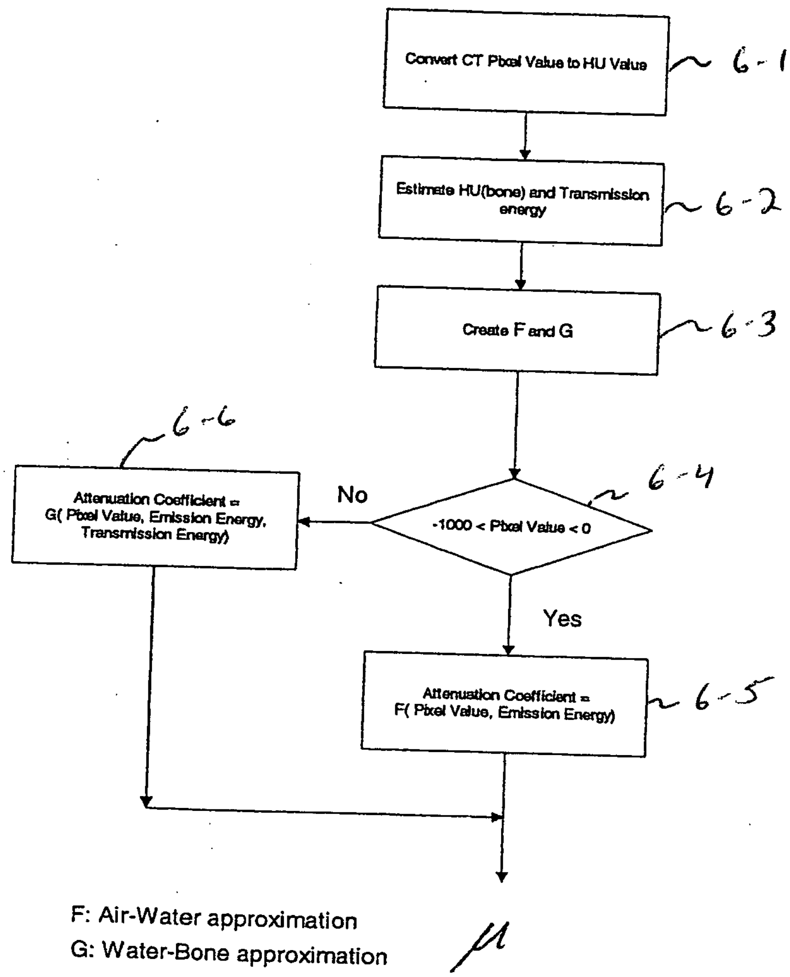
Convert CT Pixel Value to HU Value
6-1
Estimate HU(bone) and Transmission energy
6-2
Create F and G
6-3
-1000 < Pixel Value < 0
6-4
No
Yes
Attenuation Coefficient = G(Pixel Value, Emission Energy, Transmission Energy)
6-6
Attenuation Coefficient = F(Pixel Value, Emission Energy)
6-5
F: Air-Water approximation
G: Water-Bone approximation
μ

Fig. 6

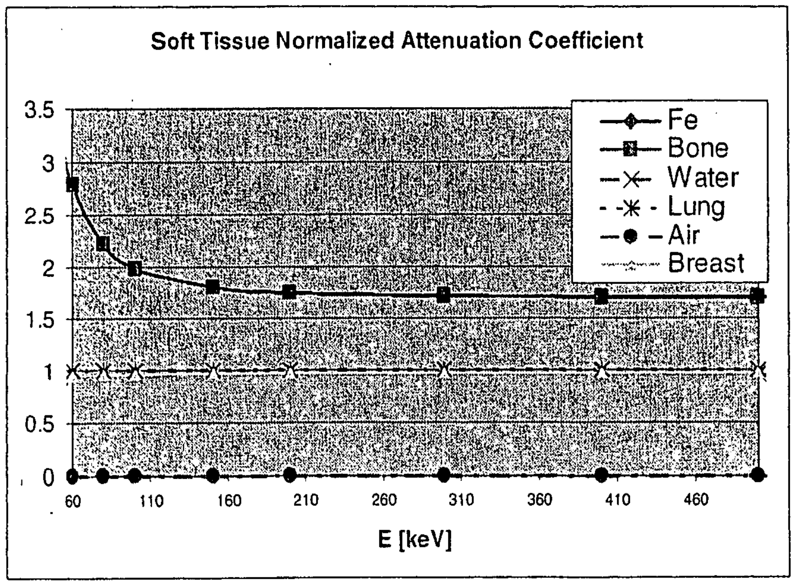

Figure 7: Soft tissue normalized linear attenuation coefficient. Linear attenuation of bone is roughly 1.75 - 2 times larger than of water and soft tissue.

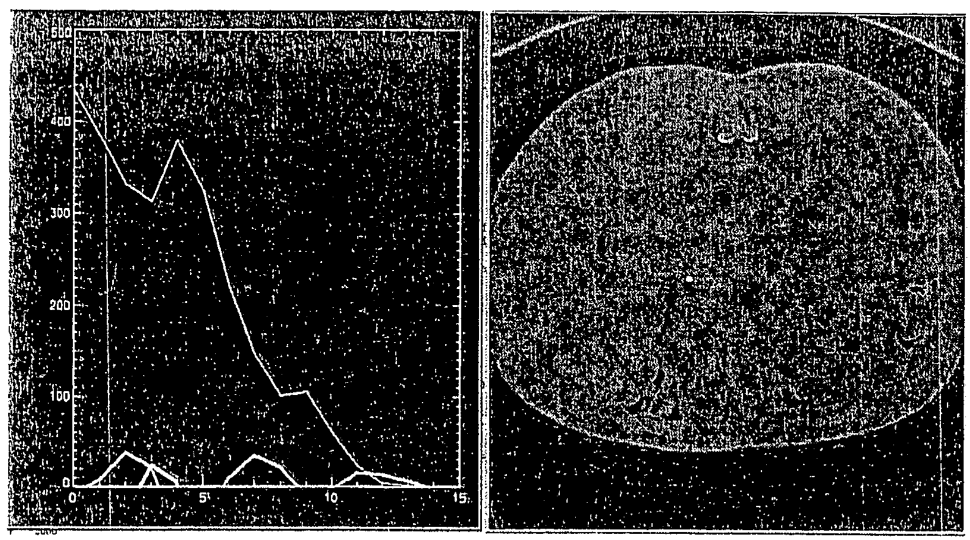

Figure 8: Slice of CT of Torso region (Kidney) and Histogram. Clear bone peak from spine at bin#=5. The lower curves show first and second derivatives.

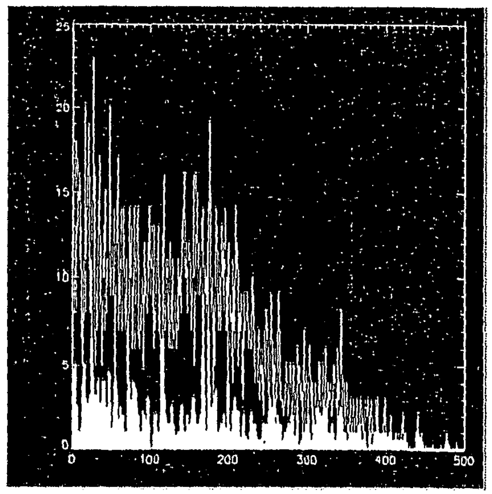

Figure 9: Histogram of the same CT volume as above (Kidney), but with 500 bins. This shows how "noisy" the data really is. The lower curves show first and second derivatives.

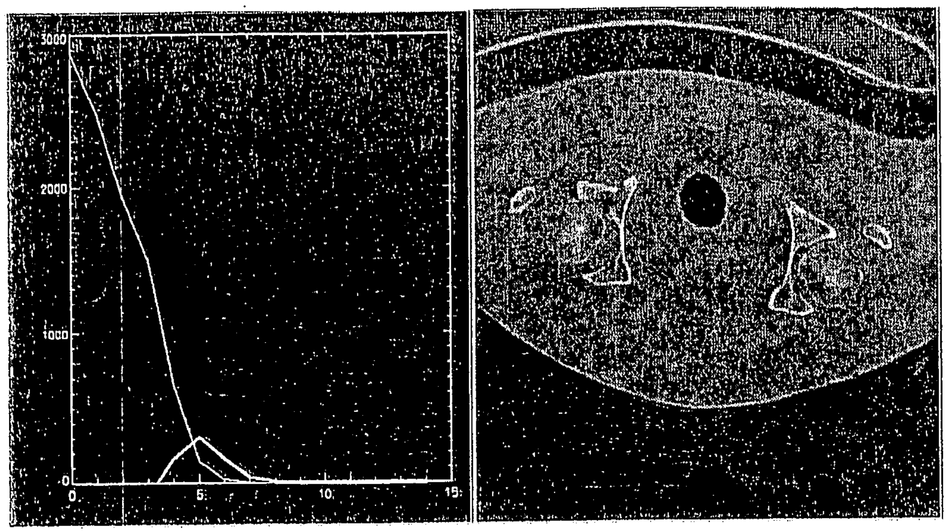

Figure 10:Slice of CT of Pelvis and Histogram. No distinct bone peak. The lower curve shows the second derivative. The location of the maximum of the second derivative is used to estimate the highest reasonable bone value.

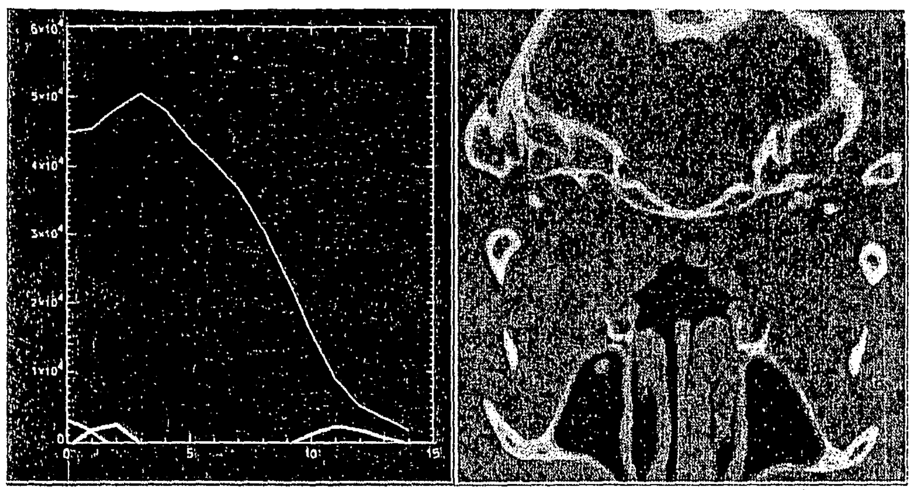

Figure 11: Slice of CT of Head and Histogram. Distinct, but wide, bone peak from the skull region. The lower curves show the first and second derivatives.

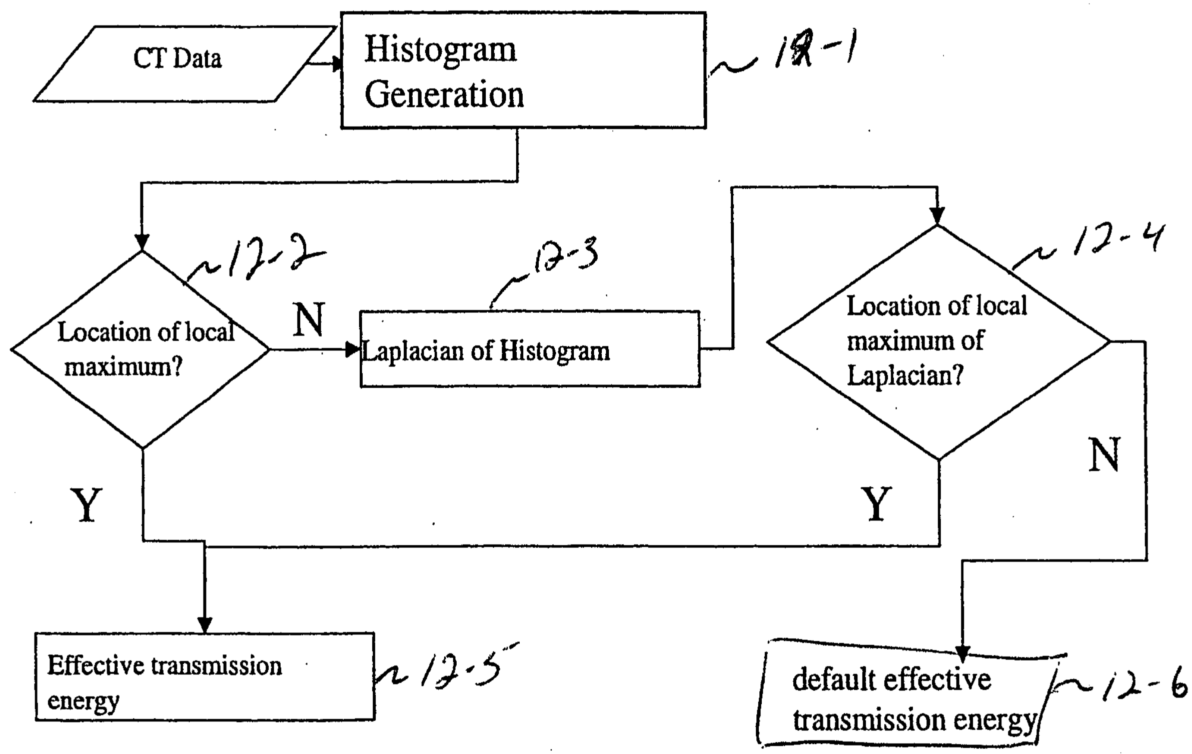

Figure 12: Flow Diagram of our implementation of the "numerical obeserver" to analyze CT data for conversion to linear attenuation coefficients.

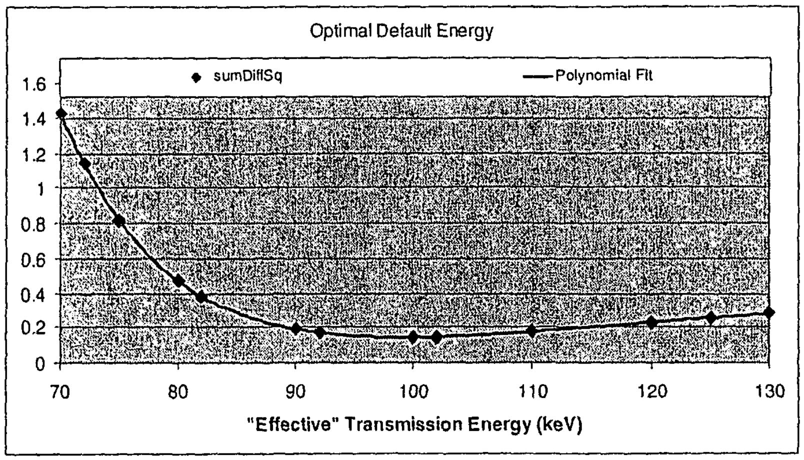

Figure 13: Optimal default effective transmission energy

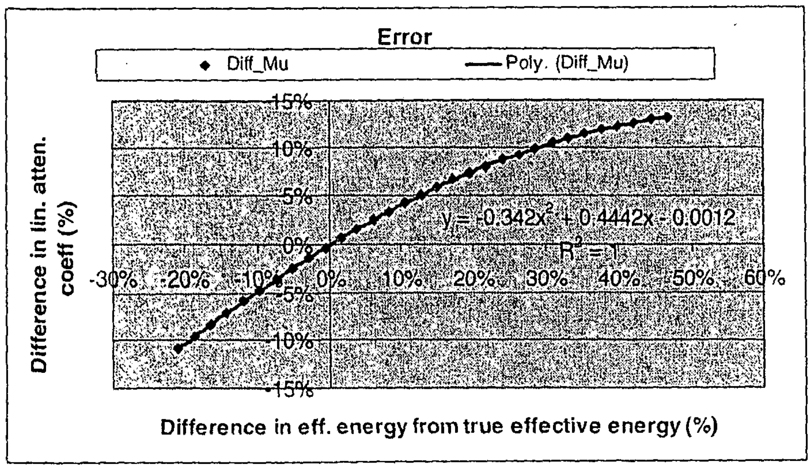

Figure 14: Error estimation. Our estimation of the effective energy is estimated to be within 10%.

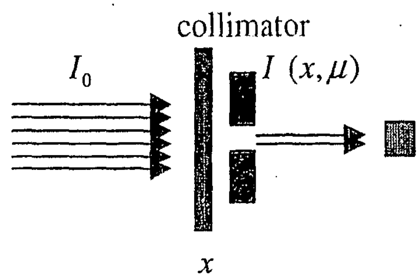

Figure 15: Attenuation of initial flux I_0 to $I(x,\mu)$ traversing an attenuating medium with linear attenuation *coefficient* μ *and* path length x.

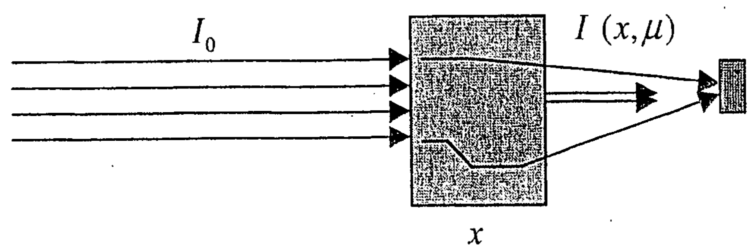

Figure 16: Broad-Beam attenuation coefficient measurement. Object scatter is allowed to enter the detector, which could be account for in an object-dependent build-up factor, not discussed here.